

Interaction Between Recovery, Recrystallization, and NbC Strain-Induced Precipitation in High-Mn Steels



LAURA LLANOS, BEATRIZ PEREDA, and BEATRIZ LÓPEZ

The interaction between recovery, recrystallization, and strain-induced precipitation in two high-Mn steels, one of them microalloyed with Nb (0.1 pct) was investigated using mechanical testing and advanced microscopy techniques. Double-hit torsion tests were carried out in the 1373 K to 1173 K (1100 °C to 900 °C) temperature range in order to characterize the fractional softening behavior. Quenched specimens were analyzed using electron backscatter diffraction and transmission electron microscopy to determine the recrystallized fraction, the precipitation state, and the austenite microstructure evolution. At the highest temperature, 1373 K (1100 °C), similar softening kinetics were found in both steels. However, at temperatures lower than 1273 K (1000 °C) for the Nb steel, strain-induced precipitation was observed to take place resulting in significant softening retardation. For the base steel at all the temperatures investigated, and for the Nb steel in the absence of strain-induced precipitation, the mechanical softening corresponded well with the recrystallized fraction. However, when strain-induced precipitation took place, a major deviation was observed denoting a significant contribution of recovery to the fractional softening. Within the deformed grains, a substructure consisting of “subgrain bands” or microbands was developed. The precipitates were found mainly on the elongated subgrain boundaries, or at dislocations within the subgrains. This configuration was maintained after the migration of the recrystallization front.

DOI: 10.1007/s11661-015-3066-2

© The Minerals, Metals & Materials Society and ASM International 2015

I. INTRODUCTION

FACED with the challenge of reduced CO₂ emissions, steel manufacturers are involved in developing new products for automotive industry with lower densities and/or higher mechanical properties. In this context, high-Mn steels characterized by TWinning-Induced Plasticity (TWIP) are highlighted because of their excellent strength and ductility combination. These steels are characterized by a high-Mn content, in the 15 to 30 pct range, and excellent strain hardening properties,^[1–4] which is attributed mainly to the formation of twins during straining. As grain boundaries, twin boundaries act as strong obstacles to dislocation motion, leading to a dynamic hardening effect and very high ductility values. Due to this effect, high-Mn steels are potentially attractive for automotive applications involving press-formed parts for energy absorption, or for structural reinforcement which assures vehicle structural stability in case of car crash.

However, crash resistance is related to Yield Strength (YS) and even fine-grained (<3 μm) TWIP alloys have naturally low YS (~450 MPa).^[2] Accordingly there is a clear benefit in increasing the yield strength of these materials. Microalloying with Nb, Ti, or V can be an

ideal hardening mechanism for doing this.^[5,6] These microalloying elements can precipitate in the form of nanometer-sized carbides and/or nitrides during the different stages of the steel production process, and, depending on the size and volume fraction of the resulting precipitate dispersion, this can lead to an increase in the steel strength at room temperature.^[7]

Several works have shown promising results concerning precipitate strengthening in TWIP steels.^[5,8,9] In addition, many works dealing with the microstructure and room temperature mechanical properties of TWIP steels have been published. However, there is much less information regarding the hot-working behavior of these steels. It must be taken into account that if strain-induced precipitation takes place during hot rolling, the amount of microalloying element available for precipitation at later stages is reduced, which can cause a loss of microalloying efficiency.^[10] Studies carried out in conventional low carbon steels indicate that increasing the Mn content results in higher solubility of microalloying elements^[11,12] and in retarded precipitation kinetics.^[13] However, at the moment, the effect of the high-Mn contents present on TWIP steels on the NbC strain-induced precipitation kinetics is not known.

Moreover, it must be taken into account that alloying elements can also interact with the softening processes which take place during hot deformation. Several works have shown that the static and dynamic softening kinetics of high-Mn steels is significantly retarded compared to low carbon steels, while the flow stress

LAURA LLANOS, Ph.D. Student, BEATRIZ PEREDA, Doctor, and BEATRIZ LÓPEZ, Professor, are with the CEIT and TECNUN (University of Navarra), P de M. Lardizabal, 15, 20018, Donostia-San Sebastián, Basque Country, Spain. Contact e-mail: blopez@ceit.es

Manuscript Submitted February 12, 2015.

Article published online August 11, 2015

and the activation energies of hot deformation and static recrystallization are higher.^[14–16] Microalloying elements can enhance these effects, leading to increased rolling loads and even more retarded softening kinetics.^[17–19] However, the effect of microalloying addition on the static softening kinetics of high-Mn steels has not been investigated so far.

In addition, research on conventional low carbon steels has shown that the interaction between softening processes (recovery and recrystallization), and microalloying elements in solid solution or as strain-induced precipitates is complex and can lead to multiple interactions.^[20,21] It should be remembered that, unlike low carbon steels, TWIP steels retain a stable austenitic microstructure after cooling to room temperature, thus allowing the high-temperature deformation microstructures to be readily characterized. As a result it is possible to analyze in detail the precipitation state and its interaction with the austenite, deformed or recrystallized, microstructure. This can provide valuable information in order to develop models of microstructure evolution during hot deformation and subsequent annealing of austenite in steels.

In this work, the softening and microstructural evolution after hot deformation of two high-Mn steels, one of them microalloyed with Nb, have been characterized. In order to do so, double-hit torsion tests have been carried out in the 1373 K to 1173 K (1100 °C to 900 °C) temperature range. Several specimens have been quenched after different holding times, and their microstructure and precipitation state analyzed in detail using the EBSD and TEM techniques.

II. EXPERIMENTAL TECHNIQUES

The chemical composition of the steels investigated is summarized in Table I. The two steels have a similar

base composition, 0.6C-20Mn-1.5Al wt. pct, but one of them is microalloyed with 0.1 pct Nb.

In order to characterize the softening behavior of the steels, double-hit torsion tests were carried out under isothermal conditions in the 1373 K to 1173 K (1100 °C to 900 °C) temperature range. The geometry of the torsion specimens was characterized by a reduced central gage section, 16.5 mm in length and 7.5 mm in diameter. Before the tests, the specimens were soaked for 10 minutes at temperatures of 1473 K (1200 °C) for the base steel and of 1523 K (1250 °C) for the Nb microalloyed steel. Next, a roughing deformation pass of $\epsilon = 0.3$ was applied at 1423 K (1150 °C) in order to obtain a refined recrystallized austenite microstructure. Finally, the specimens were cooled down to the selected test temperature, using a relatively fast cooling rate of 10 K/second to avoid premature precipitation, and deformed at a constant strain rate of 1 s^{-1} , unloaded and held for increasing times. After the interruption, the specimens were reloaded up to a $\epsilon = 0.1$ level at the same temperature. In the tests, pass-strains of 0.2 and 0.36 were employed. From the stress-strain curves, the fractional softening was determined using the 2 pct offset method.^[22]

The microstructure present before deformation was analyzed on specimens quenched after soaking-roughing-cooling cycles, selecting for this analysis the lowest deformation temperature. Specimens were also quenched after deformation and selected holding times in order to investigate the austenite microstructural evolution. The specimens were analyzed using the Electron BackScatter Diffraction (EBSD) technique in order to determine the austenite grain size and the recrystallized fraction, and carbon extraction replicas and thin foils were prepared with the aim of analyzing the precipitation state and the austenite substructure evolution. The deformation conditions and specimens selected for microstructural analysis have been

Table I. Composition of the Steels Investigated (Weight Percent)

Steel	C	Mn	Al	N	Ti	Nb
Base Steel	0.61	20.6	1.5	—	0.003	—
Nb Steel	0.63	20.3	1.2	0.0031	0.007	0.11

Table II. Deformation Conditions Employed in the Thermomechanical Tests and Specimens Selected for EBSD and TEM Analysis

Steel	Softening Kinetics		Rex. Fraction (EBSD) <i>t</i> (s)	Extraction Replicas (TEM) <i>t</i> (s)	Thin Foils (TEM) <i>t</i> (s)
	T [K (°C)]	ϵ			
Base Steel	1373 (1100)	0.36	—	—	—
	1273 (1000)		2, 6.5, 23		
	1273 (1000)	0.2	10, 37		
	1223 (950)		—		
	1173 (900)		10, 56, 228		
Nb Steel	1373 (1100)	0.36	1, 2.5, 9	—	—
	1323 (1050)		2, 10		
	1273 (1000)		10, 96, 2880		
	1223 (950)		1, 10, 96, 2880		
	1173 (900)		1, 10, 96, 2880		
			1, 10, 96, 2880		

summarized in Table II. Analysis of the quenched samples was carried out on a section corresponding to 0.9 of the outer radius of the torsion specimen, R , also known as the sub-surface section.^[23]

Orientation imaging was carried out on a Philips XL30cp scanning electron microscope with W-filament, using TSL equipment. The scans were made over a regular hexagonal grid, using step sizes of 0.5 to 1.5 μm and an analysis area of $600 \times 600 \mu\text{m}^2$ for grain size determination, and a step size of 0.5 μm and an analysis area of $250 \times 250 \mu\text{m}^2$ for recrystallized fraction calculation. Between 4 and 9 scans were recorded for each condition. These were analyzed using the TSL OIM™ Analysis 4.6 software. Grains have been defined as regions surrounded by 5 deg misorientation boundaries with a minimum grain size of 5 μm for the initial microstructure characterization, and of 1.2 μm for recrystallized fraction measurements.

Carbon extraction replicas were prepared following the standard procedure in order to analyze the size and composition of the precipitates. The precipitate size was measured in terms of the Mean Equivalent Diameter using the Digital Micrograph software. From each specimen, more than 300 precipitates were measured. Thin foils were also prepared using the lift out technique in a Quanta 3D FEG Focused Ion Beam (FIB) milling instrument. All the specimens prepared for TEM study were examined in a JEOL JEM-2100F (S)TEM microscope operated at 200 kV with a LaB₆ filament and equipped with an Oxford INCA Energy 250 Dispersive Spectrometry (EDS) system and a Gatan Imaging Filter (GIF) post-column imaging Tridiem system.

III. RESULTS

A. Initial Microstructure

In order to analyze the microstructure present before the torsion tests, EBSD maps were collected from specimens

quenched after applying soaking [1473 K to 1523 K (1200 °C to 1250 °C)], the roughing pass at 1423 K (1150 °C) and cooling down to the lowest test temperature employed, $T = 1173 \text{ K}$ (900 °C). Figure 1 shows examples of the austenite grain size maps obtained for the two steels investigated. In both cases, approximately equiaxed microstructures were found. It can also be noted that the microstructure is slightly finer in the microalloyed steel.

In the case of the Nb steel, carbon extraction replicas were also prepared from this specimen in order to characterize the initial precipitation state. In the replicas, two types of Nb precipitates were detected: cubic-shaped precipitates with an average size of $D = 120 \pm 4 \text{ nm}$, Figure 2(a), and significantly coarser irregular-shaped precipitates, some of them of size larger than 1 μm , Figure 2(b). EDS analysis (see Figure 2(c)) showed that in both cases the precipitates were mainly Nb rich, although a small amount of Ti is also present in the composition (in the EDS analysis the Cu peak arises from the grids used to hold the replicas).

B. Fractional Softening Behavior

Figures 3(a) and (b) show the fractional softening obtained for the two steels at different temperatures for a constant pass-strain of $\varepsilon = 0.36$. In Figure 3(c) the softening curves obtained for the base steel after deformation at 1273 K (1000 °C) and different strain levels are displayed. As usually observed, decreasing the deformation temperature or the pass-strain results in a delay of softening kinetics. It can also be noted that for the base steel (Figure 3(a)), at all the temperatures the softening curve follows a sigmoidal shape and can be fitted to an Avrami-type equation:

$$X = 1 - \exp\left(-0.693\left(\frac{t}{t_{0.5}}\right)^n\right), \quad [1]$$

where X is the fractional softening corresponding to a time t , $t_{0.5}$ is the time to reach 50 pct fractional softening

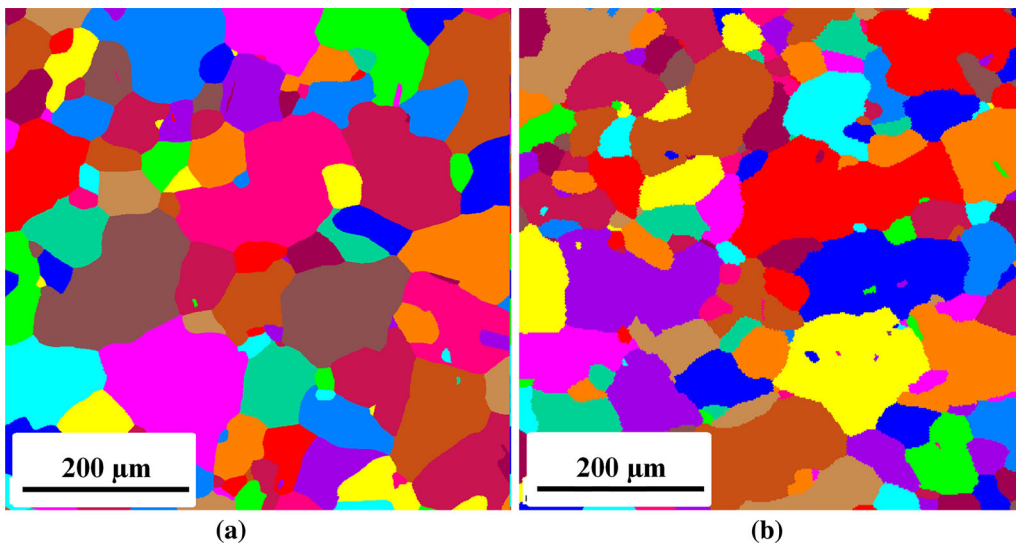


Fig. 1—Austenite grain size maps corresponding to the initial microstructure present before the torsion tests (specimens quenched after soaking and roughing). (a) Base steel, $D = 44 \pm 6 \mu\text{m}$, (b) Nb steel, $D = 31 \pm 2 \mu\text{m}$.

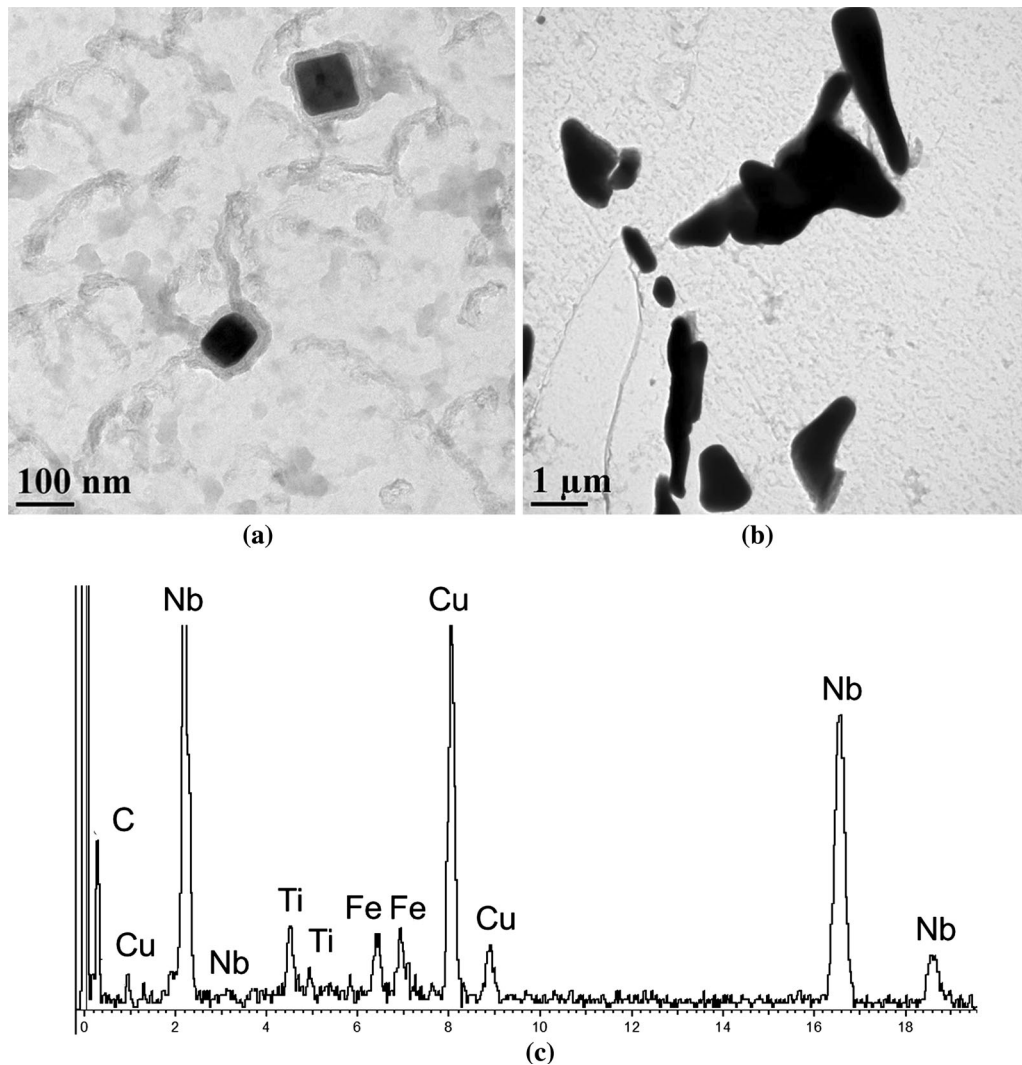


Fig. 2—(a), (b) Precipitates found in the Nb steel specimen quenched after reheating, roughing, and cooling to the lowest deformation temperature, and (c) EDS analysis corresponding to the precipitates in (b).

(s) and n is the Avrami exponent. For this steel a decrease of the n values with decreasing temperature was observed, from $n = 1.1$ at 1373 K (1100 °C) to $n = 0.7$ at 1173 K (900 °C).

For the Nb steel (Figure 3(b)), at the highest temperatures investigated, 1373 K and 1323 K (1100 °C and 1050 °C), the softening follows the same trend. However, at temperatures lower than 1323 K (1050 °C), the softening shows a larger retardation degree and does not reach completion within the interpass time range investigated. This effect is enhanced at the lowest temperature, $T = 1173$ K (900 °C), where softening levels of only ~25 pct are obtained after holding times as long as 2880 seconds.

The softening curves obtained for both steels at the different test temperatures are compared in Figure 4. As well as composition, the initial grain size can affect the softening kinetics.^[24] However, as shown above, the initial grain size obtained for both steels is similar, only slightly finer for the Nb steel (see Figure 1), and therefore the softening curves can be directly compared.

Figure 4(a) shows that at the highest temperature, 1373 K (1100 °C), the curves obtained for both steels are similar. However, at 1273 K (1000 °C) the softening obtained for the Nb steel is clearly delayed. As shown in Figure 4(b), similar trends are observed at temperatures of 1223 K and 1173 K (950 °C and 900 °C).

C. Recrystallized Fraction

Although double-deformation tests are widely employed in order to characterize the recrystallization behavior of steels, from these tests the contribution of recovery to the fractional softening cannot be completely excluded. Direct observation of the microstructure is also complicated, and the measurements obtained by classical metallography are often subjective. In the last decades, the EBSD technique has appeared as a useful tool to characterize the microstructure, and it has also been used in order to determine the recrystallized fraction. In the literature, two types of methods have been employed in order to identify the recrystallized

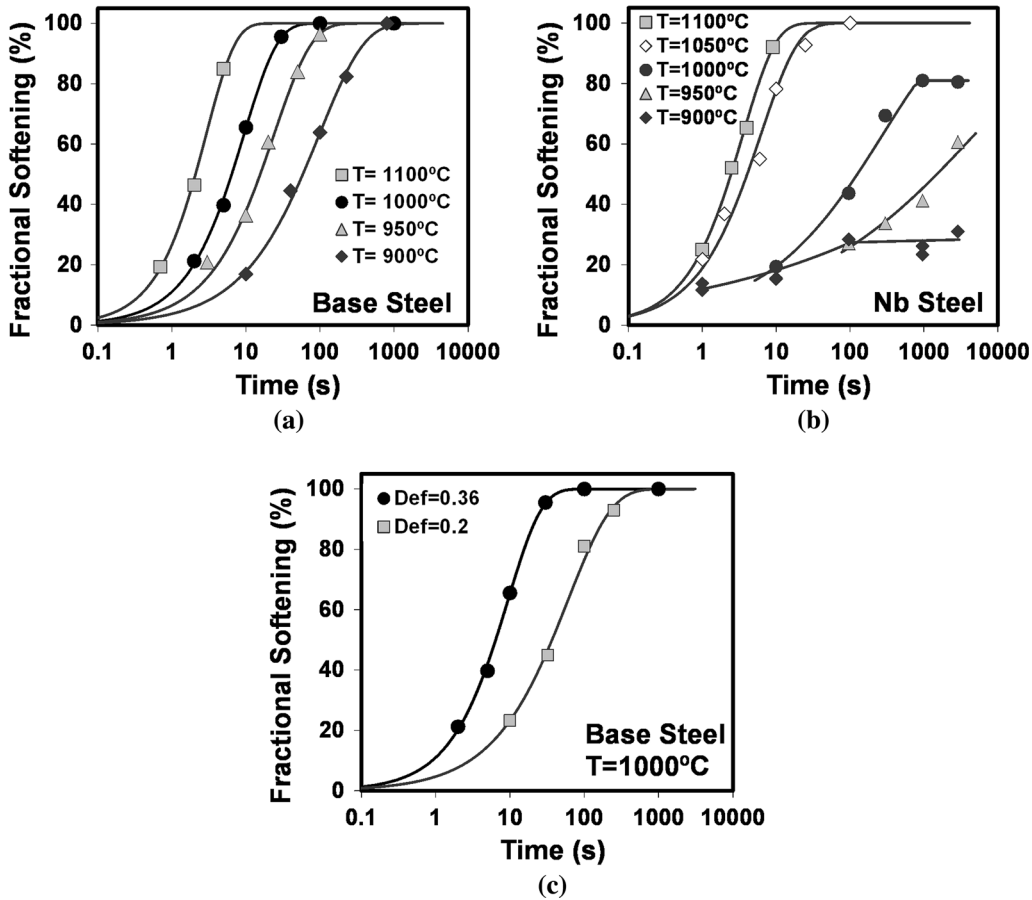


Fig. 3—Fractional softening obtained for the (a) base and (b) Nb steels at different deformation temperatures, and for the (c) base steel at different pass-strains.

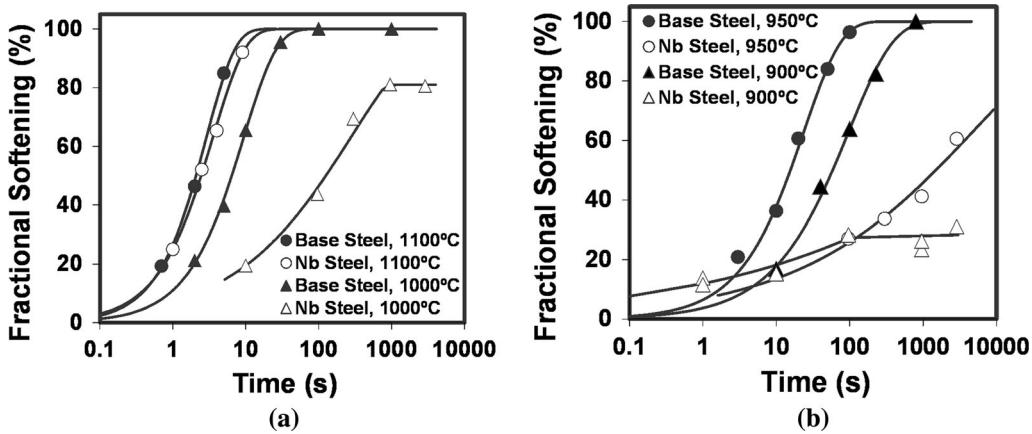


Fig. 4—Effect of steel composition on the fractional softening.

grains: Image Quality parameters^[25,26] or misorientation-based methods.^[26–29] In a previous work,^[30] we observed that for the hot deformation conditions studied in this case, Image Quality measurements were not representative of the recrystallization level. This is also in good agreement with the results reported by other authors.^[26,29] However, the Grain Orientation Spread (GOS) parameter, which is the average deviation

between the orientation of each point in a grain and the average orientation of the grain, could be used in order to distinguish the recrystallized grains from the deformed ones.

Figure 5 shows examples of the GOS parameter distributions obtained for the Nb microalloyed steel deformed at 1273 K (1000 °C) after different holding times. During hot deformation, the crystal structure of

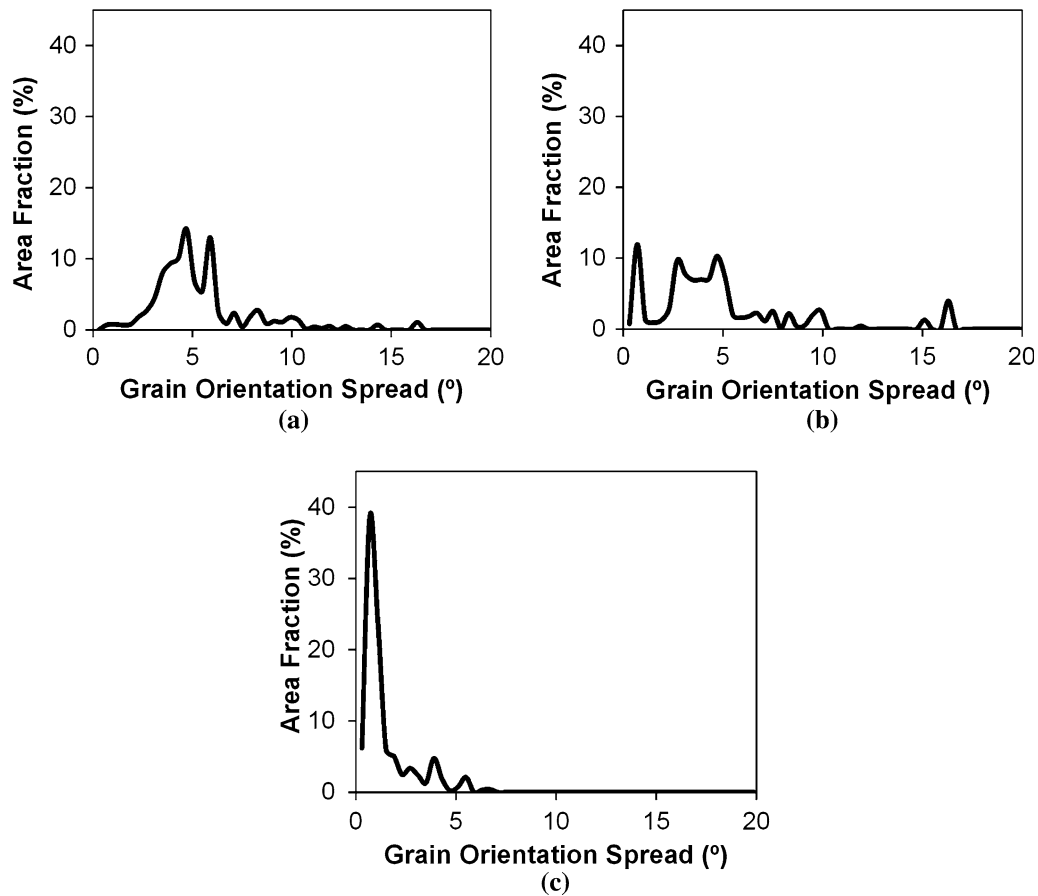


Fig. 5—GOS parameter distributions obtained for the Nb steel deformed at 1273 K (1000 °C) after different holding times: (a) 10 s, (b) 96 s, (c) 2880 s.

the material is distorted. After deformation, if recrystallization occurs new grains free of deformation and with uniform inside orientation are formed. This is reflected in Figures 5(a) through (c). It can be observed that for the shortest holding time, $t = 10$ s, which corresponds to a specimen with a relatively low softening fraction, $FS \approx 20$ pct, the GOS parameter distribution is relatively wide with most grains with high intragranular misorientation values (>1.5 deg), characteristic of a deformed microstructure. As the holding time increases, the distributions become narrower, with a significant increase in the number of grains with low GOS values (<1.5 deg), which can be associated with recrystallized grains. One of the limitations of this method is that there is not an established GOS limit value for the definition of a recrystallized grain. Field *et al.*^[28] reported that values from 1 to 3 deg gave similar recrystallized fraction results for deformed and annealed copper, and selected a threshold value of 2 deg for recrystallized grain identification, while a value of 1 deg was used by Mandal *et al.*^[29] for a hot deformed Ti-modified austenitic stainless steel. These values are in good agreement with that observed in the distributions of Figures 5(a) through (c). In the present study, GOS limiting values between 1 and 2 deg were selected without significant differences. A maximum value of 1.5 deg was finally chosen for the identification of the recrystallized grains.

Figures 6 and 7 show examples of the IQ maps obtained for the two steels investigated after deformation at 1173 K and 1273 K (900 °C and 1000 °C), respectively. In the Image Quality maps, the recrystallized areas calculated from the GOS measurements have been drawn superimposed in blue. A fairly good correspondence can be observed between the zones defined as recrystallized by the software and those indicated by the morphological characteristics typically used in conventional optical microscopy, such as the grain size and shape (equiaxed or elongated) differences.

From Figures 6(a) and (d), it can be observed that after deformation at 1173 K (900 °C) and a short holding time of 10 seconds, the two steels present slightly elongated deformed microstructures. Defects within the grains and serrations in the grain boundaries can also be detected. In addition, in the case of the base steel (Figure 6(a)), the first recrystallized grains can be found in the microstructure, mainly located at triple junctions and grain boundaries. For this steel, as the interpass time increases from 10 to 56 seconds, a significant increase of the recrystallized fraction takes place (Figure 6(b)). As usually observed, the recrystallization process shows a large degree of heterogeneity and the recrystallized grains appear grouped in clusters or mainly in bands. By increasing the interpass time up to $t = 228$ seconds (Figure 6(c)), for the base steel an equiaxed microstructure with a high recrystallization

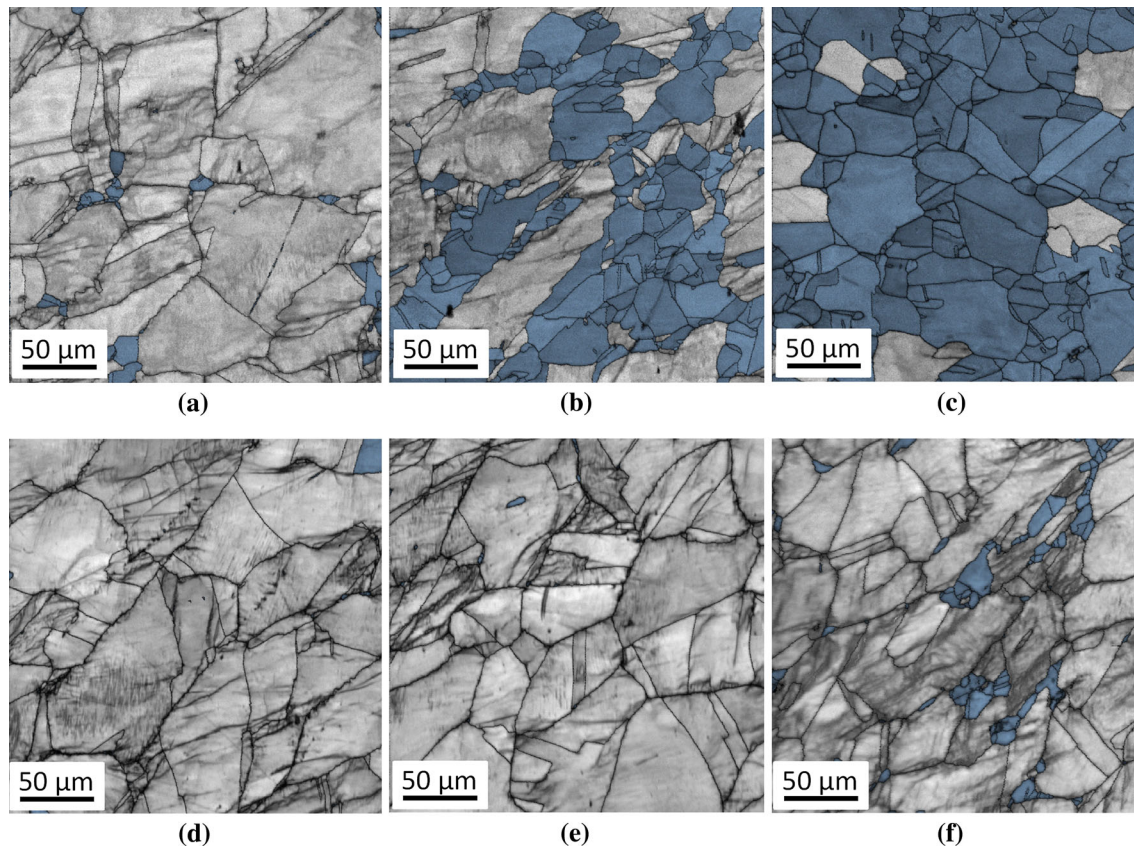


Fig. 6—IQ+GOS maps corresponding to the base and Nb steels after deformation at 1173 K (900 °C) and different holding times. (a) Base steel, 10 s, $F_{\text{Rex}} = 4.1$ pct, (b) Base steel, 56 s, $F_{\text{Rex}} = 43.8$ pct, (c) Base steel, 228 s, $F_{\text{Rex}} = 84.8$ pct, (d) Nb steel, 10 s, $F_{\text{Rex}} = 0.5$ pct, (e) Nb steel, 96 s, $F_{\text{Rex}} = 0.6$ pct, (f) Nb steel, 2880 s, $F_{\text{Rex}} = 5.7$ pct.

degree is obtained. As expected, such microstructure is refined compared to the initial one. On the other hand, in the case of the Nb steel increasing the interpass time from 10 to 96 seconds (Figure 6(e)) does not produce significant changes in the microstructure. Only after a holding time of 2880 seconds (Figure 6(f)), the first recrystallized grains can be detected.

The microstructures observed in specimens quenched after deformation at 1273 K (1000 °C) and short interpass times, (Figures 7(a) and (d)), show features similar to the above case. That is, the microstructure appears slightly elongated and defects within the grains are clearly distinguished. For the base steel, the first recrystallized grains can already be detected in 2 seconds. For this steel, by increasing the interpass time to 23 seconds (Figure 7(c)) a high recrystallized fraction level of $F_{\text{Rex}} = 83$ pct is reached. In the case of the Nb steel, the recrystallized fraction also tends to increase with interpass time. However, the holding time needed to achieve a high recrystallized fraction is significantly longer, $t = 2880$ seconds, ($F_{\text{Rex}} = 74$ pct in Figure 7(f)).

The recrystallized fraction values measured for both steels at the different deformation conditions are summarized in Table III.

D. Strain-Induced Precipitation

In order to investigate the strain-induced precipitation kinetics, replicas extracted from Nb steel specimens quenched after deformation were investigated. The conditions selected for analysis are summarized in Table II.

At the highest temperature [$T = 1323$ K (1050 °C)], a specimen quenched 10 s after deformation, which corresponds to a 84 pct recrystallized fraction (see Table III), was firstly analyzed. The replicas extracted from this specimen showed a precipitation state similar to the initial microstructure, *i.e.*, only coarse precipitates were detected. This means that after deformation at 1323 K (1050 °C) recrystallization is nearly complete before significant strain-induced precipitation occurs.

At lower temperatures, the replicas extracted from specimens quenched 1 second after deformation showed also a similar precipitation state. However, when increasing the holding time to 10 seconds, a significant amount of strain-induced precipitates could be detected. This indicates that for the Nb steel, strain-induced precipitation is initiated at holding times between 1 and 10 seconds in the 1273 K to 1173 K (1000 °C to 900 °C) temperature range. This is in good agreement with the large softening retardation observed at these temperatures (see Figure 4).

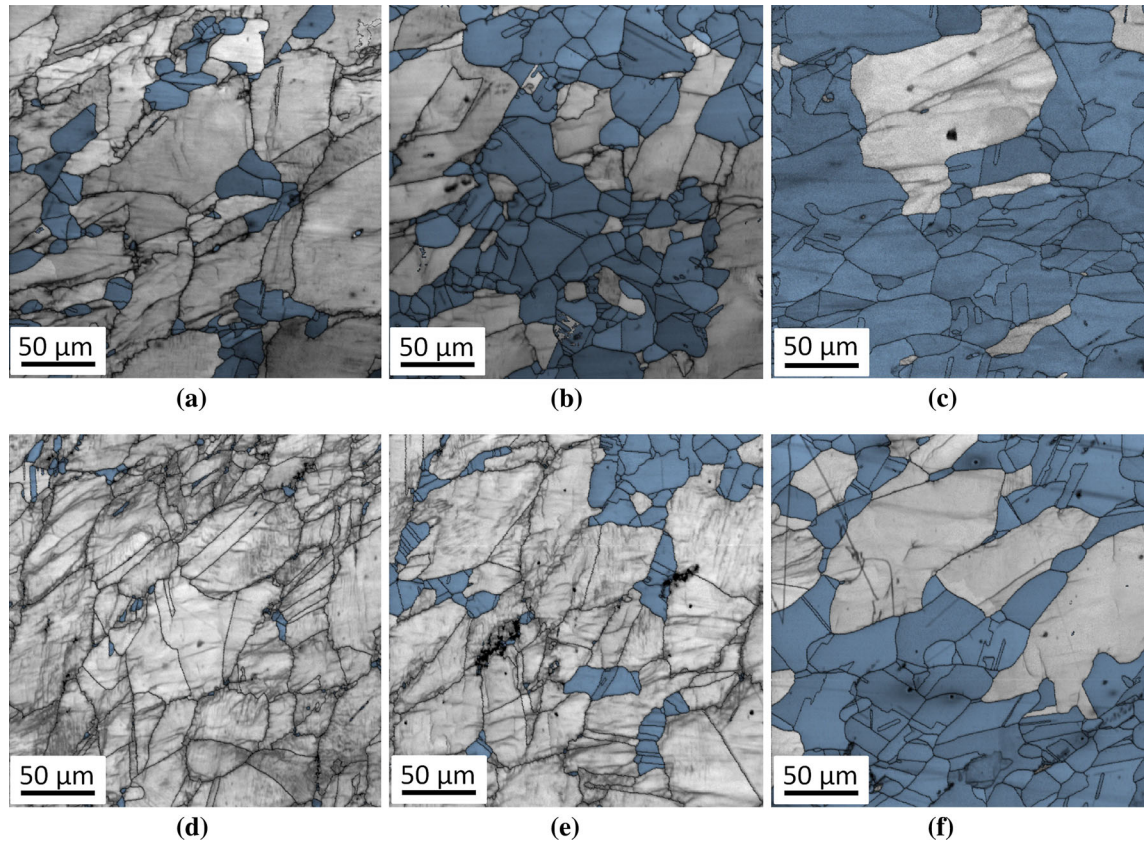


Fig. 7—IQ+GOS maps corresponding to the base and Nb steels after deformation at 1273 K (1000 °C) and different holding times. (a) Base steel, 2 s, $F_{\text{Rex}} = 11.3$ pct, (b) Base steel, 6.5 s, $F_{\text{Rex}} = 55.7$ pct, (c) Base steel, 23 s, $F_{\text{Rex}} = 83.0$ pct, (d) Nb steel, 10 s, $F_{\text{Rex}} = 2.0$ pct, (e) Nb steel, 96 s, $F_{\text{Rex}} = 14.4$ pct, (f) Nb steel, 2880 s, $F_{\text{Rex}} = 74.2$ pct.

Table III. Recrystallized Fraction Measured by EBSD Means from the Quenched Specimens

Steel	ϵ	T_{Def} [K (°C)]	t (s)	F_{Rex} (Pct)	
Base	0.2	1273 (1000)	10	1.9	
			37	58.0	
	0.36	1273 (1000)	2	11.3	
			6.5	55.7	
			23	83.0	
			1173 (900)	10	4.1
Nb	0.36	1373 (1100)	56	43.8	
			228	84.8	
			1	29.7	
		1323 (1050)	2.5	52.7	
			9	96.2	
			2	17.0	
	1273 (1000)	10	10	84.0	
			96	14.4	
		2880	2880	74.2	
			1223 (950)	1	0.8
		1173 (900)	10	10	0.8
				96	1.7
2880	2880		26.2		
	10		0.5		
	96	0.6			
	2880	5.7			

Examples of the precipitates extracted after deformation at temperatures from 1273 K to 1173 K (1000 °C to 900 °C) and holding times from 10 to 2880 seconds are shown in Figure 8. The mean precipitate size measured in each specimen has also been included in the figure. As shown in the micrographs, in all the cases the precipitates can be easily detected within the carbon replicas. In addition, it can be noted that these strain-induced precipitates ($D = 6.9$ to 24.9 nm) are significantly finer than the coarse precipitates present in the initial microstructure (see Figure 2), and therefore, they can be easily distinguished. The figure also indicates that the precipitate size tends to increase with increasing temperature and/or interpass time. However, this effect is enhanced at the highest temperatures; at 1273 K (1000 °C) the precipitate size increases from $D = 12.4$ to 24.9 nm when time increases from $t = 10$ to 2880 seconds (Figures 8(a) and (c)), while at 1173 K (900 °C) it remains nearly constant, $D = 7.4$ to 8.4 nm (Figures 8(g) and (i)).

Although the precipitate size can be directly measured from the replicas, estimation of the precipitate volume fraction is more complicated. It has been reported that the efficiency of precipitate extraction is unknown, and can vary from replica to replica by a factor of two.^[31] In addition, precipitate agglomerates such as the ones

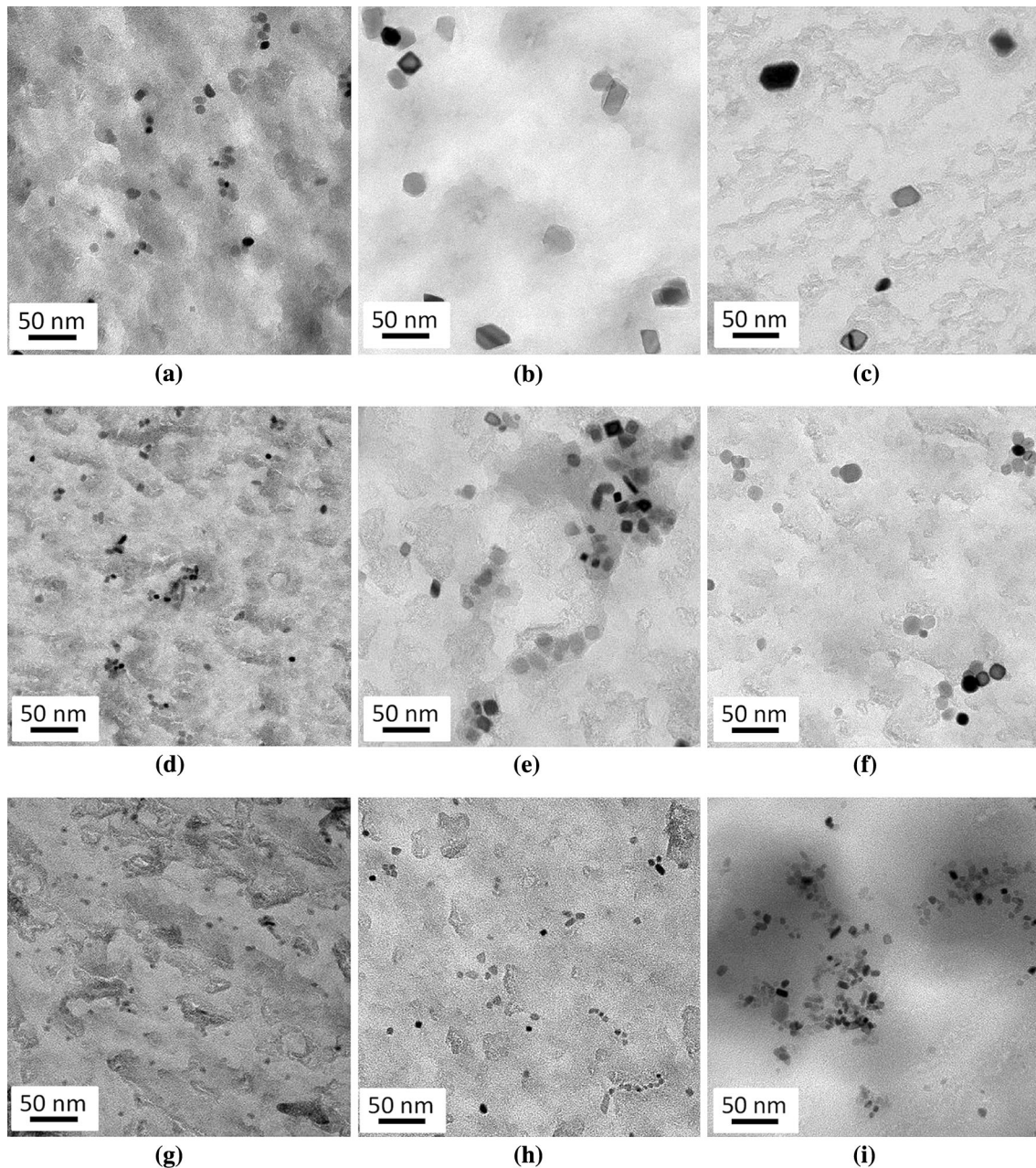


Fig. 8—Strain-induced precipitates observed in Nb steel specimens quenched at different conditions. (a) $T = 1273$ K (1000 °C), 10 s, FS = 20 pct, $D = 12.4 \pm 0.7$ nm, (b) $T = 1273$ K (1000 °C), 96 s, FS = 44 pct, $D = 22.5 \pm 0.4$ nm, (c) $T = 1273$ K (1000 °C), 2880 s, FS = 80 pct, $D = 24.9 \pm 0.9$ nm, (d) $T = 1223$ K (950 °C), 10 s, $D = 6.9 \pm 0.1$ nm, (e) $T = 1223$ K (950 °C), 96 s, FS = 26 pct, $D = 13.3 \pm 0.4$ nm, (f) $T = 1223$ K (950 °C), 2880 s, FS = 61 pct, $D = 18.6 \pm 0.6$ nm, (g) $T = 1173$ K (900 °C), 10 s, FS = 15 pct, $D = 7.4 \pm 0.2$ nm, (h) $T = 1173$ K (900 °C), 98 s, FS = 28 pct, $D = 7.9 \pm 0.2$ nm, (i) $T = 1173$ K (900 °C), 2880 s, FS = 31 pct, $D = 8.4 \pm 0.2$ nm.

present in Figures 8(e) or (i) are an artifact arising from the replica preparation method and are not representative of the specimen precipitation state, as is further discussed below. However, the micrographs suggest that at 1273 K and 1223 K (1000 °C and 950 °C) the precipitate density tends to decrease with interpass time, especially at the largest interpass times investigated. This could be attributed to the occurrence of precipitate coarsening processes during the isothermal holding. On the other hand, at 1173 K (900 °C) the precipitate density tends to increase with interpass time, while the

precipitate size remains almost constant. With decreasing temperature, Nb diffusion rate is reduced, and therefore, precipitate growth and coarsening rate decreases and can even be inhibited. In addition, it has been reported that the migration of the recrystallization front can increase precipitate coarsening rate.^[32] The recrystallization levels obtained after interpass times of $t = 2880$ seconds are significantly larger at 1273 K (1000 °C) ($F_{\text{Rex}} = 74$ pct) than at 1173 K (900 °C) ($F_{\text{Rex}} = 6$ pct) and therefore, this could also contribute to the observed behavior.

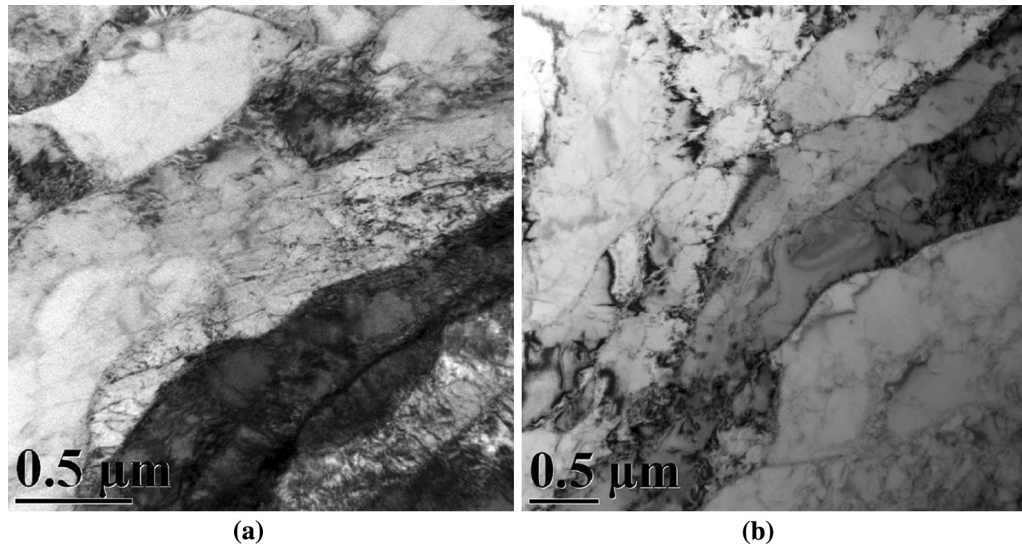


Fig. 9—Deformed microstructure observed in the thin foils prepared from the Nb specimen deformed at 1223 K (950 °C) and quenched after: (a) 1 s; (b) 96 s holding time.

E. Microstructure Evolution

In order to further analyze the austenite microstructural evolution and its interaction with strain-induced precipitation process, thin foils were prepared from several Nb steel specimens. The samples selected for this analysis were those quenched after deformation at 1223 K (950 °C) and holding times of 1, 96 and 2880 seconds.

After 1 second holding time, in all the thin foils analyzed, a deformed microstructure was observed. Although in some grains more random substructures were observed, in most of them, microbands or “subgrain bands”,^[33] similar to those shown in the micrographs of Figure 9(a), were identified. As the figure shows, inside some of the subgrains, dislocations, and even a rudimentary cell structure can be detected. At this condition, strain-induced precipitates were not detected in any of the thin foils analyzed.

After 96 seconds, the microstructure consisted also of grains with elongated microband substructure, as shown in Figure 9(b). However, in the thin foils strain-induced precipitates could be detected. Figures 10(a) and (b) show that in some cases these could be directly observed in the Bright Field images of the microstructure. It can be noted from Figure 10(b) (red arrows) that around some of the precipitates deformation contrast, which is characteristic of coherent and semi-coherent precipitates,^[32] is present.

In other cases, Dark Field images (Figure 11) were collected in order to image the precipitates. It must be mentioned that due to the small precipitate size only some of the spots of the precipitate diffraction pattern could be detected. However, in all the cases, the position of the precipitate spots with respect to the deformed matrix diffraction pattern was in good accordance with the cube-cube orientation relationship $((001)_{\gamma} // (001)_{\text{NbC}}, [100]_{\gamma} // [100]_{\text{NbC}})$, which is usually reported for B1-type carbides with respect to austenite.^[32] This also agrees

well with the strain contrast observed around the precipitates.

As shown in Figure 12, the precipitates could also be imaged through the EFTEM technique, using the three window method.^[34] The maps were obtained using the Nb-N_{2,3} edge, following conditions similar to those described in Reference 35. It can be observed that the Nb precipitates show a very good contrast in the map; however, in order to obtain good quality maps the thickness of the foils is critical (thickness $\lesssim 100$ nm), and the observation area is generally reduced as compared to Dark Field imaging. From the three figures, it can be observed that the precipitates were found mainly located at dislocations within the subgrains (Figure 10) or at subgrain boundaries (Figures 11 and 12).

After 2880 seconds, in the foils recrystallized grains, recognizable by the absence of substructure, could be observed. An example is shown in Figure 13. As the figure shows, a significant amount of precipitates were also present in the recrystallized grains.

In this specimen, recrystallization migration fronts could also be detected. Figure 14 shows an example of recrystallized (Figures 14(a) and (b)) and deformed (Figures 14(c) and (d)) grains located at both sides of the recrystallization front. Within the deformed zones the microband substructure is conserved, appearing the precipitates decorating the subgrain boundaries, or inside the subgrain at dislocations. It can be noted that in the recrystallized grain, the precipitates are also aligned in rows, despite the absence of substructure.

IV. DISCUSSION

A. Initial Microstructure

Figure 1 shows that for the two steels investigated, the initial microstructure obtained after the roughing pass

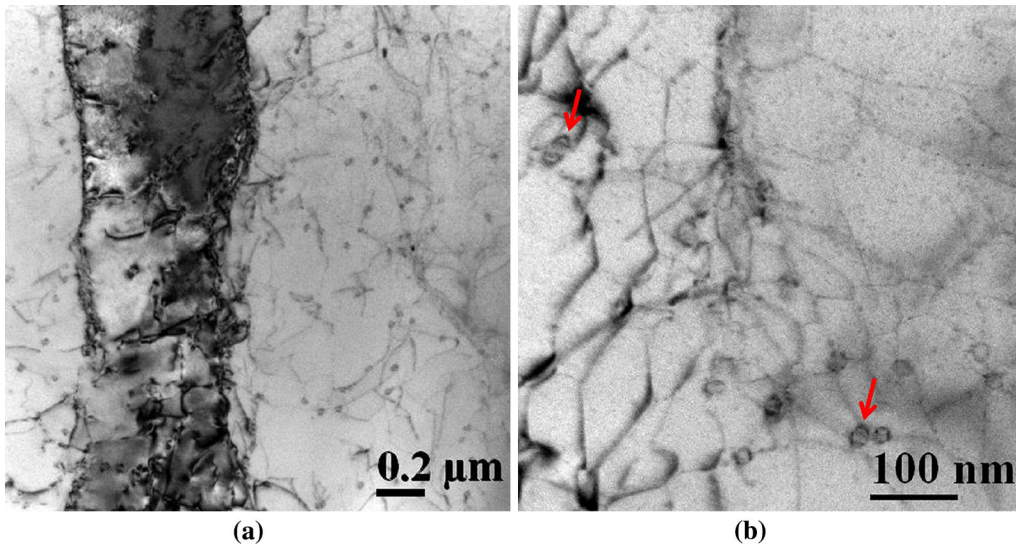


Fig. 10—Precipitates found at dislocations within the subgrains in the Nb specimen deformed at 1223 K (950 °C) and quenched after 96 s holding (Color figure online).

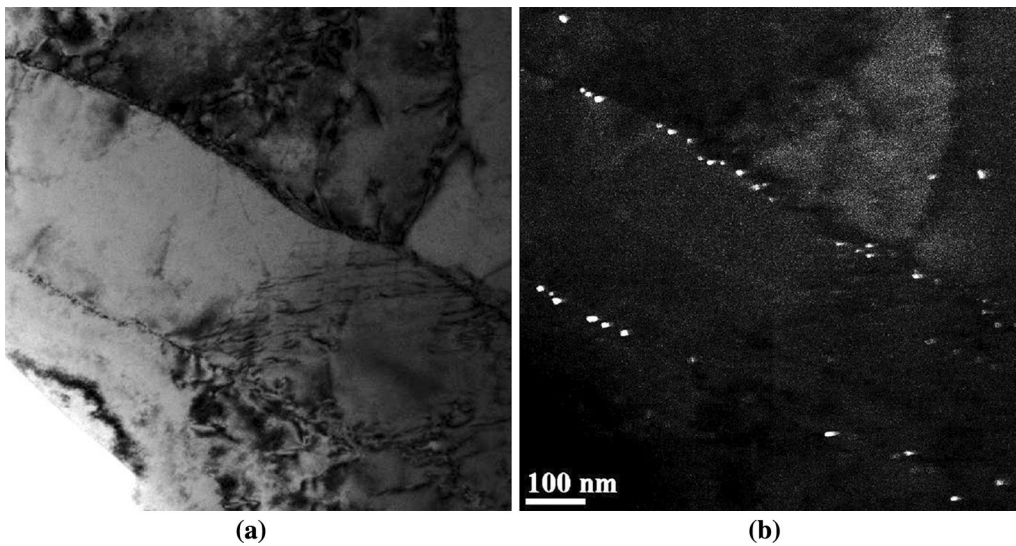


Fig. 11—(a) Bright field and (b) dark field images of foil corresponding to the Nb specimen deformed at 1223 K (950 °C) and quenched after 96 s holding showing precipitates at the subgrain boundaries.

consists of recrystallized equiaxed grains. It can also be noted that although the soaking temperature was larger for the Nb steel [$T = 1523$ K (1250 °C)] than for the base steel [$T = 1473$ K (1200 °C)], the microstructure is slightly finer in the microalloyed steel. This can be attributed to the effect of Nb in solid solution, or to the significant amount of coarse Nb-based precipitates found in the initial microstructure for this steel (Figure 2).

Examination of the microstructure of the original cast confirmed that these coarse precipitates were present in the original material and, therefore, were not dissolved during reheating. This is in good accordance with the thermodynamic predictions of the software Thermo-Calc.^[36] Figure 15 shows the amount of Nb in solid solution (wt. pct) in the austenite predicted by the

software for the Nb steel at different temperatures. The calculations were performed using a database valid for High-Mn steels developed in a recent work.^[37] It can be observed that after reheating at 1523 K (1250 °C), only less than half of the Nb present in the Nb microalloyed steel (0.041 pct) is dissolved, and thus, is available for further precipitation. In addition, the small amount of Ti present in the particles (see EDS in Figure 2(c)), which arises from the residual content of Ti in the steel (Table I), can also contribute to decrease the solubility of these precipitates. The calculations also indicate that increasing reheating temperature could lead to larger Nb dissolution levels. However, it should be noted that the melting temperature predicted for this steel by the software is relatively low [≈ 1613 K (1340 °C)], and below the temperature for precipitate dissolution.

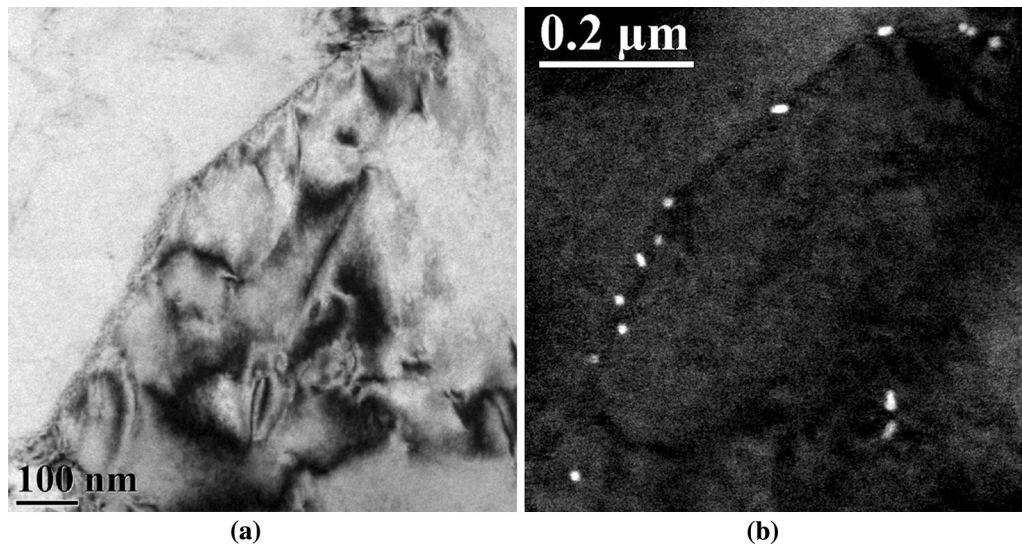


Fig. 12—(a) Bright field and (b) three window Nb-N_{2,3} edge map corresponding to the Nb specimen deformed at 1223 K (950 °C) and quenched after 96 s holding showing precipitates at the subgrain boundaries.

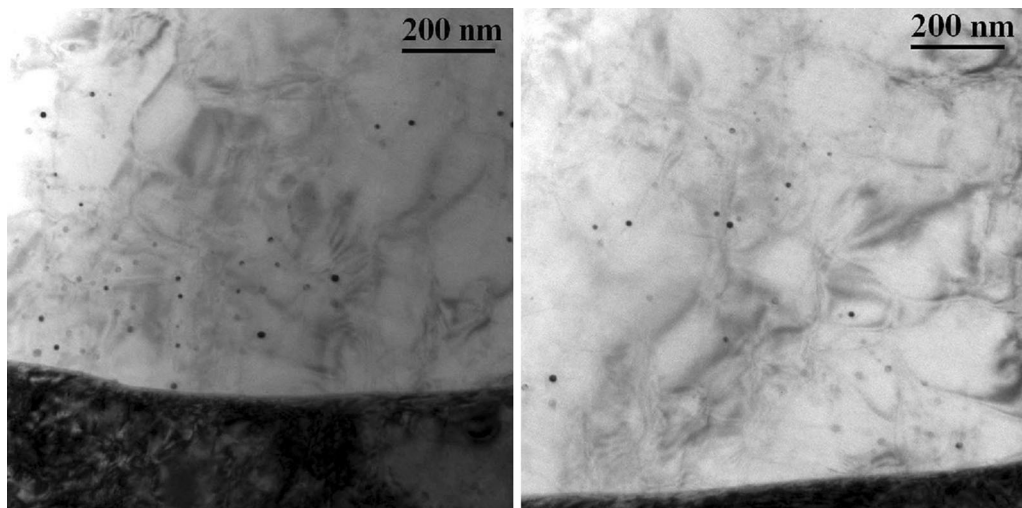


Fig. 13—Examples of precipitates observed in recrystallized grains in the Nb steel specimen deformed at 1223 K (950 °C) quenched after 2880 s.

Regarding the effect of these precipitates on the fractional softening, it is well known that small precipitates (<20 nm) can retard or even inhibit softening processes. However, due to their large size, these coarse undissolved precipitates are not expected to significantly affect the softening behavior of the steels investigated.^[38]

B. Microstructural Evolution

The EBSD measurements indicate that after deformation at 1223 K (950 °C) and a holding time of 1 second, for the Nb steel recrystallization process is not initiated ($F_{\text{Rex}} < 1$ pct). In good agreement with this, all the thin foils analyzed at this condition show a deformed microstructure, as it can be observed in Figure 9(a). At

this condition, strain-induced precipitates were not detected in any of the thin foils/replica analyzed.

As shown in Figure 9(a), for this hot-deformed austenitic steel, within most of the grains, a deformation substructure consisting of banded subgrains or microbands was observed. Similar substructures have also been observed after hot deformation in other austenitic alloys, such as Ni-30 pct Fe deformed in torsion,^[39,40] 316L austenitic stainless steel after hot rolling,^[41] and Fe-30 pct Ni deformed in plane strain compression conditions.^[42,43] This is also the predominant substructure observed in the non-cube oriented grains for AISI 304 for deformation temperatures larger than 973 K (700 °C) and Ni-30 pct Fe steels subjected to plane strain and uniaxial compression.^[33,44,45] As in the case of

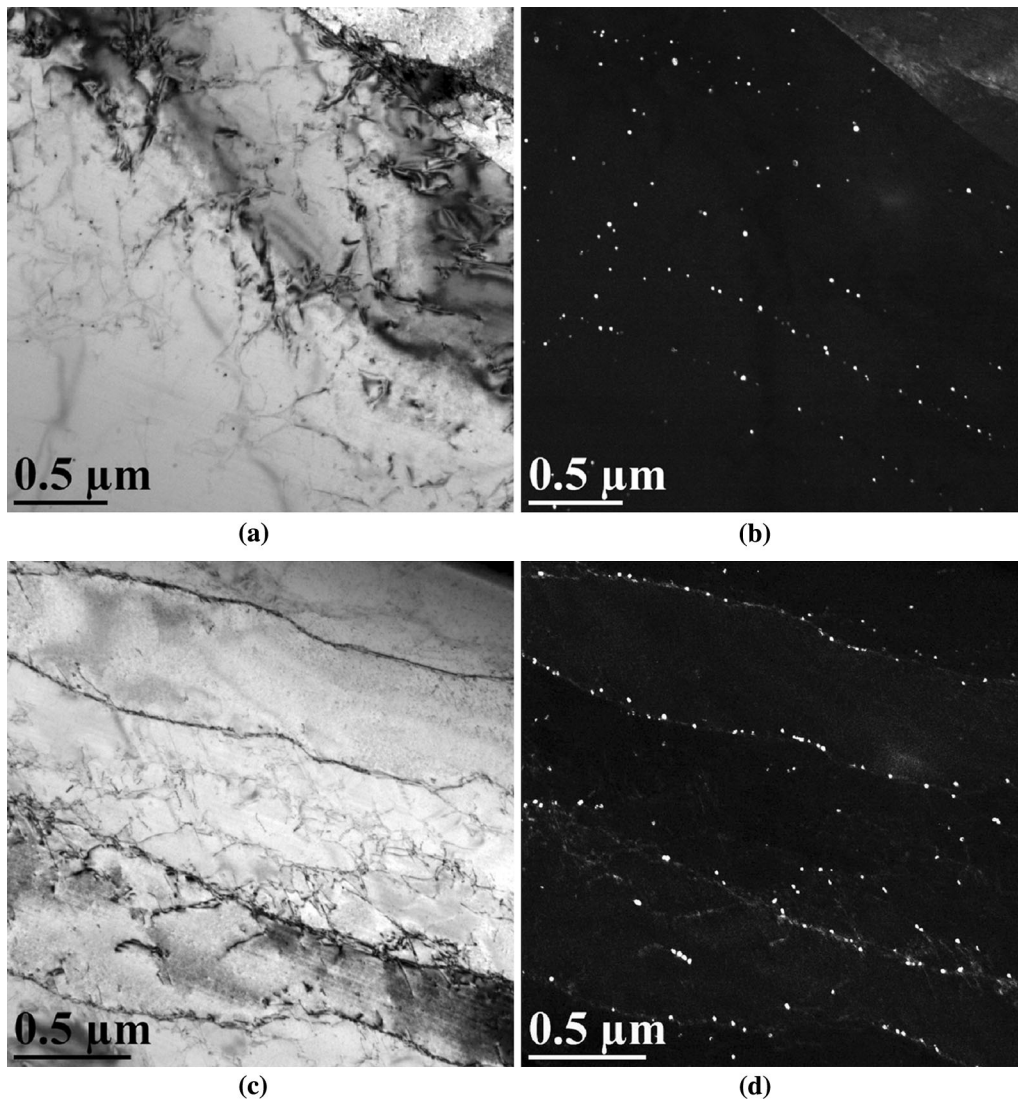


Fig. 14—Microstructure observed in a thin foil corresponding to a specimen of the Nb steel deformed at 1223 K (950 °C) and quenched after 2880 s holding time at both sides of the recrystallization front: (a) Bright and (b) dark field image of a recrystallized grain; (c) bright and (d) dark field images of the contiguous deformed grain.

Reference 44, it can be observed from the micrographs that the microband boundaries are not always strictly planar, and their projected width varies locally. It must be mentioned that despite the limited resolution of the EBSD maps, the microbands could also be noticed in some of the grains (see for example Figure 6(d)).

In specimens subjected to plane strain compression, the microbands have been found to be mostly aligned at angles of 20 to 50 deg to the elongation direction.^[33] In the case of torsion, it has been reported that these tend to be aligned parallel to the plastic flow direction,^[39] although in some cases they display significant deviations.^[46] In the present case, the microbands were found aligned with the direction normal to the torsion axis, or at intermediate angles between the normal to the torsion axis and the deformation direction, thus deviated from the plastic flow direction. The origin of the arrangement of these microbands is not well known; some works

suggest that the microband walls tend to form along well-defined crystallographic planes with highly concentrated slip, while in other cases it has been suggested that the dislocation wall alignment is essentially non-crystallographic and that these walls have a tendency to align themselves parallel to the most stressed macroscopic planes.^[39,46,46]

After 96 seconds holding time, the fractional softening measured from the double-hit torsion tests is $FS \approx 28$ pct (Figure 3(b)). However, the EBSD analysis indicates that the recrystallized fraction is significantly lower ($F_{\text{Rex}} = 1.7$ pct). In good accordance with the EBSD measurements, in all the thin foils analyzed a deformed banded subgrain substructure was observed (Figure 9(b)). Also in agreement with the replica results, which indicate that at these conditions strain-induced precipitation starts at times between 1 and 10 seconds, precipitates could be observed in the thin foils. These were found mainly located at the subgrain boundaries or

at dislocations within the subgrains (Figures 10 through 12). Similar results have been reported for hot-deformed austenitic Fe-30Ni alloys.^[42,43]

It is interesting to note that the shape and size of the precipitates in the thin foils agrees well with those observed in the carbon extraction replicas (Figure 8(e)).

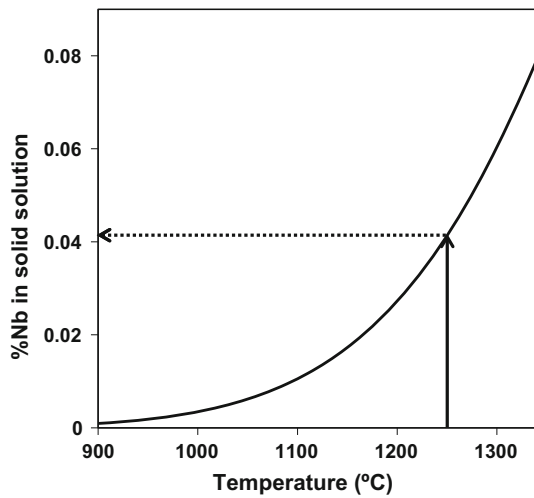


Fig. 15—Amount of Nb in solid solution (wt pct) in the austenite calculated with the Thermo-Calc software as a function of temperature for the Nb steel.^[36,37] The reheating temperature employed in the tests is also marked in the figure.

The precipitate size measured from Nb elemental maps taken randomly in the thin foils (see one in Figure 12), $D = 15.7$ nm, is close to the precipitate size determined from the carbon replicas, $D = 13.3$ nm. On the other hand, the precipitate agglomerates found in the carbon replicas were not observed in the thin foils, confirming that this is an artifact of the carbon extraction replica preparation method.

At the longest time investigated, $t = 2880$ seconds, a recrystallized fraction of $F_{\text{Rex}} = 26$ pct (FS ≈ 60 pct) was measured. Accordingly, in the thin foils, recrystallized grains, such as the ones shown in Figures 13 or 14(a) and (b) can be detected. It was observed that in the recrystallized grains the precipitates were abundant. As shown in Figure 14, in some cases, despite the absence of substructure, they appear arranged in rows. It is believed that these precipitates were formed at subgrain boundaries in the deformed grains and maintain their configuration after the pass of the recrystallization migration front. The recrystallized grain shown in Figure 14(a) was contiguous to the deformed grain of Figure 14(c) (a small portion of the deformed grain can be observed in the upper right corner of the Figure 14(a)). The precipitates in the recrystallized grain are aligned parallel to the subgrain band substructure present in the deformed grain. As mentioned above, due to their small size, the diffraction pattern of the precipitates was difficult to obtain. However, it should be mentioned that in this case the Dark Field images of

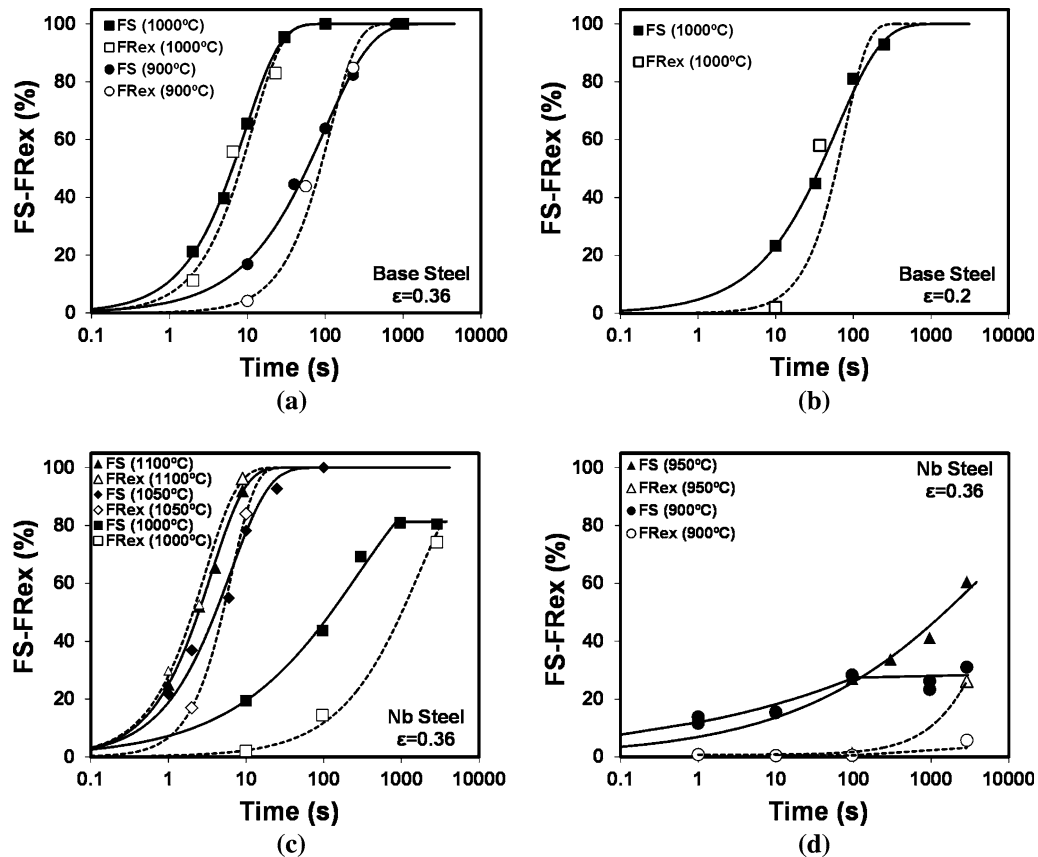


Fig. 16—Fractional softening and recrystallized fraction determined by EBSD means for the steels studied in this work.

the precipitates in the recrystallized and the unrecrystallized grains could be simultaneously obtained using the diffraction spots of the deformed grain precipitates. This suggests that the precipitates were similarly oriented in the two grains, which could be expected if these were originally formed in the same deformed grain.

C. Softening-Recrystallization-Precipitation Interaction

Figure 16 shows the softening curves obtained for the two steels compared with the recrystallized fraction data obtained by EBSD means. Figures 16(a) and (b) show that for the base steel there is a good correspondence between the fractional softening and the recrystallized fraction, independently of the deformation conditions. Only at the first softening stages a deviation of approximately 10 to 20 pct can be observed, this being slightly larger for the lowest strain ($\epsilon = 0.2$). For the Nb steel, at the highest temperatures investigated, 1373 K and 1323 K (1100 °C and 1050 °C), similar trends are observed.

These results agree well with those obtained by Fernandez *et al.*^[22] for a low carbon Nb microalloyed steel. They observed that after deformation at 1373 K (1100 °C), the softening determined by the 2 pct offset method corresponded well with the recrystallized fraction determined by conventional optical microscopy. Similar results have also been obtained recently for a TRIP-type steel alloyed with 1 pct Al level.^[47] In this work, it was observed that at low softening levels the experimental and model recrystallization data were slightly below the softened fraction (~20 pct), but at larger softening levels both values tended to converge. Therefore, the results suggest that at high-temperature conditions, when strain-induced precipitation does not take place, the 2 pct offset method can be effectively employed in order to estimate the recrystallized fraction.

It is interesting to note that at 1373 K (1100 °C), the softening curves obtained for the base and Nb steels are similar (see Figure 4(a)). This indicates that in these conditions Nb in solid solution does not affect the softening kinetics of these TWIP steels. This is in contrast with the results usually reported for conventional low carbon steels. In that case, Nb in solid solution is known to lead to significant retardation of the recrystallization processes due to solute drag effect.^[48]

Hamada *et al.*^[14,15] have shown that the softening kinetics of high-Mn steels is retarded compared to low carbon steels. The experimental times required to reach a 50 pct recrystallized fraction, $t_{0.5}$, derived from the softening curves of Figure 3 at high temperatures, have been compared with the predictions of the equation proposed by Fernandez *et al.*^[49] for C-Mn and Nb-Ti microalloyed low carbon steels with lower Mn contents. Experimental times are between 2 and 3 times longer than those predicted by the equation for similar grain size and deformation conditions. The mechanism leading to this retardation could be related to the contribution of solute drag of Mn and also Al^[47,50] in reducing grain boundary mobility. Since the solute drag mechanism can show saturation effects for high alloying

contents, this would explain the lack of effect observed in the softening kinetics due to Nb addition in solid solution in the presence of such high-Mn contents.

At temperatures lower than 1323 K (1050 °C), for the Nb steel, the interaction between softening and recrystallization is more complex. At these temperatures, strain-induced precipitation was observed to take place between 1 and 10 seconds, leading to significant softening retardation (see Figure 4). To the authors knowledge, the effect of strain-induced precipitation on the softening or recrystallization behavior of High-Mn steels has not been investigated in deep. In the case of low carbon Nb microalloyed steels, strain-induced precipitation start is associated to the appearance of halts or “plateaux” in the softening curves. The beginning of the plateau is theoretically related to the time for 5 pct of the equilibrium precipitate volume fraction at the corresponding temperature. Nevertheless, it has also been observed that the beginning of the plateau can be associated to a higher precipitated volume fraction. Iparraguirre *et al.*^[51] reported values ranging between 14 and 27 pct of the equilibrium precipitate volume fraction. Figures 16(c) and (d) show that for the steels analyzed, although the softening and recrystallization curves are significantly delayed, softening saturations are not present in all cases. At 1273 K (1000 °C), the softening fraction tends to increase continuously with increasing interpass time following a sigmoidal shape up to interpass times of about 1000 seconds. At 1223 K (950 °C), the fractional softening continuously increases within the interpass time range investigated. Only at the lowest temperature, the softening levels tend to saturate after 100 seconds holding time.

As previously mentioned in the introduction, several authors have pointed out that increasing the Mn content results in higher solubility of microalloying elements and therefore, retarded precipitation kinetics.^[11-13] In the present case, for the Nb steel relatively fast strain-induced precipitation kinetics is observed. At temperatures from 1173 K to 1273 K (900 °C to 1000 °C), precipitation is observed to start at times between 1 and 10 seconds. A direct comparison of these data with

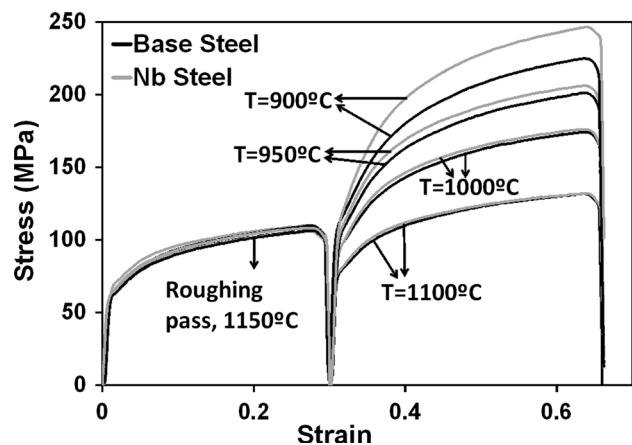


Fig. 17—Stress-strain curves obtained during roughing and during the first deformation pass in tests carried out with the two steels investigated at different deformation temperatures.

those corresponding to low carbon Nb microalloyed steels is difficult since the carbon content of the present Nb steel is much higher. It is expected that this could significantly accelerate precipitation kinetics compared to low carbon steels having similar Nb contents. Further studies are necessary in order to assess the effect of high-Mn levels on precipitation kinetics.

In addition, it is interesting to note that at these temperatures [1173 K to 1273 K (900 °C to 1000 °C)], a significant deviation between softening and recrystallization is observed. As well as recovery and recrystallization, if strain-induced precipitation takes place, precipitate hardening and/or reduction of solid-solution hardening can affect the stress-strain curves and therefore, the calculated mechanical fractional softening.^[20,21] Precipitation hardening has been observed to lead to a significant stress increase^[45] and can result in “humps” in the softening curves.^[20,52] However, the opposite effect is observed here; that is, the softening levels tend to be larger than the recrystallized fraction. This effect could be attributed to the loss of Nb solid-solution hardening due to strain-induced precipitation.

In order to analyze the potential of Nb as solid-solution hardener during hot deformation, the stress-strain curves obtained for the base and Nb steels at different conditions have been compared in Figure 17. In the graph, the first curve corresponds to the roughing pass given at 1423 K (1150 °C), and the second one to the first curve of the double-hit deformation test. It must be remembered that strain-induced precipitation was found to take place during the holding time between the first and second deformation curves of the double-hit torsion tests. Therefore, at the conditions shown in Figure 17 only very coarse precipitates (see Figure 2) were present in the microstructure of the Nb steel, which are expected to have a weak strengthening effect. It can be observed that at temperatures from 1423 K to 1273 K (1150 °C to 1000 °C) the stress-strain curves are similar for both steels. This indicates that at these conditions Nb in solid solution does not affect the stress values. Decreasing the temperature to 1223 K (950 °C) the stress level of the Nb steel slightly increases with respect to the base steel, this increment being enhanced at 1173 K (900 °C). Since strain-induced precipitation was only observed to take place after deformation this stress increment can only be due to the hardening effect of Nb in solid solution. According to the figure, the hardening effect is enhanced as the temperature decreases. This means that a loss of Nb in solid solution caused by precipitation during the interpass interval could in fact reduce the hardening effect associated to this element and thus explain, in part, the deviation between mechanical softening and recrystallization observed at 1173 K (900 °C). As above mentioned, this solute hardening decrease could be partially compensated by the hardening effect associated to strain-induced precipitates formed during the interpass interval, which is reported to be more pronounced than the former. However, it should be taken into account that this would in fact lead to a lower difference between mechanical softening and recrystallization.

Data shown in Figures 17(c) through (d) indicate that at 1273 K and 1223 K (1000 °C and 950 °C) there is also a significant deviation between softening and recrystallization. At these temperatures, Nb solid-solution hardening is weak (see Figure 17); therefore this deviation can only be explained by the action of recovery during the isothermal holding time. A precipitate dispersion can provide a pinning force that can affect both the progress of recrystallization and recovery. However, it seems that in the present case, strain-induced precipitation results in a larger effect on the recrystallization process than on recovery. It is interesting to note that, according to the TEM results, at 1223 K (950 °C) the microband microstructure is conserved within the deformed grains up to the longest interpass times investigated. Therefore, at least at this temperature, recovery progress can be mainly attributed to the annihilation and/or rearrangement of dislocations within the microbands.

It is difficult to determine if this significant contribution of recovery to the fractional softening when strain-induced precipitation takes place is characteristic of the High-Mn steels investigated in this work. The amount of data available in the literature for low C steels relating to softening and recrystallization is limited, mainly due to the difficulty of revealing the austenite microstructure. Nevertheless, it must be mentioned that a similar effect was observed by Kang *et al.*^[52] for a low carbon Nb microalloyed steel when strain-induced precipitation took place.

Finally, it is interesting to analyze the effect of the strain-induced precipitates on the recrystallization process. It is known that precipitates can retard or even stop recrystallization progression due to Zener pinning drag effect. This happens when the precipitates exert a pinning force on the migrating grain boundary which counteracts the driving force for recrystallization. The drag force is increased by decreasing precipitate size or increasing precipitate volume fraction.^[38] In the present case, at temperatures from 1173 K to 1273 K (900 °C to 1000 °C), at short interpass times ($t = 10$ seconds) the precipitates are relatively small ($D = 7$ to 12 nm), which results in high Zener pinning drag forces. However, at 1273 K (1000 °C), and also at 1223 K (950 °C), although to a lower extent, with increasing interpass time precipitate coarsening can occur. This results in a decrease of the Zener force, and as a result, recrystallization can proceed.

On the other hand, it must be remembered that precipitates can also stop recrystallization by preventing the nucleation stage. It is interesting to note that at temperatures from 1273 K to 1173 K (1000 °C to 900 °C), not only progression, but also recrystallization start is retarded. In addition, a significant amount of strain-induced precipitates is observed before recrystallization initiates. TEM analysis showed that at 1223 K (950 °C), after 96 seconds, before recrystallization is initiated ($F_{\text{Rex}} = 1.7$ pct), strain-induced precipitates could be observed within the microstructure, mainly located at subgrain boundaries. Clearly, these precipitates can also exert a pinning effect on the subgrain boundaries preventing subgrain growth and therefore, retarding

nucleation. From the results obtained, it is difficult to determine which of the two mechanisms, grain or subgrain boundary pinning is the mechanism responsible for the observed recrystallization retardation effect.

V. CONCLUSIONS

1. The interaction between softening, recrystallization, and strain-induced precipitation in two high-Mn steels, one of them microalloyed with Nb, was investigated. At high temperatures both the base and the Nb microalloyed steel show a significant retardation of the recrystallization time, $t_{0.5}$, compared to the predictions of an equation previously developed for steels with lower Mn contents. This delay can be attributed to the effect of the high Mn content of these steels. Additionally, the relatively high Al content of the analyzed steels could also contribute to delay kinetics. At 1373 K (1100 °C), the addition of Nb, which is in solid solution at this temperature, does not produce any additional retardation of softening kinetics with respect to the base steel. In contrast, at temperatures lower than 1323 K (1050 °C), strain-induced precipitation occurs in the Nb steel at interpass times between 1 and 10 seconds, leading to a large softening retardation. Nevertheless, halts or stops on the softening curves are not observed at times corresponding to strain-induced precipitation start.
2. For the base steel at all the temperature range investigated, and for the Nb steel at high temperatures, *i.e.*, in the absence of strain-induced precipitation, the mechanical softening determined by the 2 pct offset method correlated fairly well with the recrystallized fraction determined by EBSD means. However, when strain-induced precipitation takes place, 2 pct offset fractional softening values are significantly larger than the measured recrystallized fractions. Although some deviations between mechanical softening and recrystallized fraction could be attributed to changes in state of solute or precipitated Nb in relation to its hardening effects, here observed behavior seems to be mainly due to the operation of recovery. This indicates that at these conditions strain-induced precipitation has a larger effect on retarding recrystallization than recovery.
3. Within the deformed grains, a substructure consisting of “subgrain bands” or microbands was observed. Strain-induced precipitates were found mainly located at the subgrain boundaries or at dislocations within the subgrains and maintain this configuration after the migration of the recrystallization front.

ACKNOWLEDGMENT

The authors acknowledge financial support from the European Union, Research Programme of the Re-

search Fund for Coal and Steel (RFSR-CT-2010-00018).

REFERENCES

1. B.C. DeCooman, K. Chin, J. Kim: in *New trends and Developments in Automotive System Engineering*, M. Chiaberge, ed., In-Tech, Rijeka, Croatia, 2011, pp. 101–28.
2. O. Bouzaiz, S. Allain, C.P. Scott, and P. Cugy: *Curr. Opin. Solid St. M.*, 2011, vol. 15, pp. 141–68.
3. C. Scott, S. Allain, M. Faral, and N. Guelton: *La Revue Metall. CIT*, 2006, vol. 103, pp. 293–302.
4. G. Frommeyer, U. Brux, and P. Neumann: *ISIJ Int.*, 2003, vol. 43, pp. 438–46.
5. C. Scott, B. Remy, J.L. Collet, A. Cael, C. Bao, F. Danoix, B. Malard, and C. Curfs: *Int. J. Mater. Res.*, 2011, vol. 102, pp. 538–49.
6. A. Grajcar, M. Opiela, and G. Fojt-Dynamara: *Arch. Civ. Mech. Eng.*, 2009, vol. 9, pp. 49–58.
7. T. Gladman: *Mater. Sci. Technol.*, 1999, vol. 15, pp. 30–36.
8. J.P. Chateau, A. Dumay, S. Allain, and A. Jacques: *J. Phys. Conf. Ser.*, 2010, vol. 240, pp. 1–4.
9. H. Yen, M. Huang, C.P. Scott, and J. Yang: *Scripta Mater.*, 2012, vol. 6, pp. 1018–23.
10. C. Klinkenberg, K. Hulka, and W. Bleck: *Steel Res. Int.*, 2004, vol. 75, pp. 744–52.
11. S. Koyama, T. Ishii, and K. Narita: *J. Jpn. Inst. Met.*, 1971, vol. 35, pp. 1089–94.
12. F. Siciliano and J.J. Jonas: *Metall. Mater. Trans. A*, 2000, vol. 31A, pp. 511–30.
13. M.G. Akben, I. Weiss, and J.J. Jonas: *Acta Metall.*, 1981, vol. 29, pp. 111–21.
14. A.S. Hamada, L.P. Karjalainen, and M.C. Somani: *ISIJ Int.*, 2007, vol. 47, pp. 907–12.
15. A.S. Hamada, L.P. Karjalainen, and M.C. Somani: *Mater. Sci. Eng. A*, 2007, vol. 467A, pp. 114–24.
16. N. Cabañas, N. Akdut, J. Penning, and B.C. De Cooman: *Metall. Mater. Trans. A*, 2006, vol. 37A, pp. 3305–15.
17. A. Grajcar, R. Kuziak, and W. Zalecki: *Arch. Civ. Mech. Eng.*, 2012, vol. 12, pp. 334–41.
18. F. Reyes-Calderon, I. Mejia, and J.M. Cabrera: *Mater. Sci. Eng. A*, 2013, vol. 562A, pp. 46–52.
19. F. Reyes-Calderon, I. Mejia, A. Boulaajn, and J.M. Cabrera: *Mater. Sci. Eng. A*, 2013, vol. 560A, pp. 552–60.
20. H.S. Zurob, C.R. Hutchinson, Y. Brechet, and G. Purdy: *Acta Mater.*, 2002, vol. 50, pp. 3075–92.
21. H.S. Zurob, C.R. Hutchinson, Y. Brechet, and G.R. Purdy: *Mater. Sci. Eng. A*, 2004, vol. 382A, pp. 64–81.
22. A.I. Fernandez, B. Lopez, and J.M. Rodriguez Ibabe: *Scripta Mater.*, 1999, vol. 40, pp. 543–49.
23. G. Glover and C.M. Sellars: *Metall. Trans.*, 1972, vol. 3, pp. 2271–80.
24. F. Humphreys and M. Hatherly: *Recrystallization and Related Annealing Phenomena*, 2nd ed., Elsevier Ltd., Oxford, 2004, p. 227.
25. J. Tarasiuk, Ph. Gerber, and B. Bacroix: *Acta Mater.*, 2002, vol. 50, pp. 1467–77.
26. S. Mitsche, P. Poelt, and C. Sommitsch: *J. Microsc.*, 2007, vol. 227, pp. 267–74.
27. H. Lu, P. Sivaprasad, and C.H.J. Davies: *Mater. Character.*, 2003, vol. 51, pp. 293–300.
28. D.P. Field, L.T. Bradford, M.M. Nowell, and T.M. Lillo: *Acta Mater.*, 2007, vol. 55, pp. 4233–41.
29. S. Mandal, A.K. Bhaduri, and V.S. Sarma: *Metall. Mater. Trans. A*, 2011, vol. 42A, pp. 1062–72.
30. L. Llanos, B. Pereda, D. Jorge-Badiola, J.M. Rodriguez-Ibabe, and B. López: *Mater. Sci. Forum*, 2013, vol. 753, pp. 443–48.
31. M.F. Ahsby and R. Ebeling: *T. Metall. Soc. AIME*, 1966, vol. 236, pp. 1396–404.
32. Y. Yazawa, T. Furuhashi, and T. Maki: *Acta Mater.*, 2004, vol. 52, pp. 3727–36.
33. A.S. Taylor, P. Cizek, and P.D. Hodgson: *Acta Mater.*, 2011, vol. 59, pp. 5832–44.

34. P.J. Thomas and P.A. Midgley: *Top. Catal.*, 2002, vol. 21, pp. 109–38.
35. E. Courtois, T. Epicier, and C. Scott: *Micron*, 2006, vol. 37, pp. 492–502.
36. J.O. Andersson, T. Helander, L. Hoglund, P.F. Shi, and B. Sundman: *CALPHAD*, 2002, vol. 26, pp. 273–312.
37. PrecHiMn-04 database (RFSR-CT-2010-00018).
38. M. Gomez, S.F. Medina, and P. Valles: *ISIJ Int.*, 2005, vol. 45, pp. 1711–20.
39. H. Beladi, P. Cizek, and P.D. Hodgson: *Acta Mater.*, 2010, vol. 58, pp. 3531–41.
40. H. Beladi, P. Cizek, and P.D. Hodgson: *Metall. Mater. Trans. A*, 2009, vol. 40A, pp. 1175–89.
41. P. Cizek, J.A. Whiteman, W.M. Rainforth, and J.H. Beynon: *J. Microsc.*, 2004, vol. 213, pp. 285–95.
42. W.M. Rainforth, M.P. Black, R.L. Higginson, E.J. Palmiere, C.M. Sellars, I. Prabst, P. Warbichler, and F. Hofer: *Acta Mater*, 2002, vol. 50, pp. 735–47.
43. V. Nagarajan, E.J. Palmiere, and C.M. Sellars: *Mater. Sci. Technol.*, 2009, vol. 25, pp. 1168–74.
44. A.S. Taylor, P. Cizek, and P.D. Hodgson: *Acta Mater.*, 2012, vol. 60, pp. 1548–69.
45. D. Poddar, P. Cizek, H. Beladi, and P.D. Hodgson: *Acta Mater.*, 2014, vol. 80, pp. 1–15.
46. P. Cizek, H. Beladi, A.S. Taylor, and D. Peter Hodgson: *Mater. Sci. Forum*, 2013, vol. 753, pp. 54–57.
47. Z. Aretxabaleta, B. Pereda, and B. López: *Metall. Mater. Trans.*, 2014, vol. 45A, pp. 934–47.
48. H.L. Andrade, M.G. Akben, and J.J. Jonas: *Metall. Trans. A*, 1983, vol. 14, pp. 1967–77.
49. A.I. Fernandez, P. Uranga, B. López, and J.M. Rodriguez-Ibabe: *ISIJ Int.*, 2000, vol. 40, pp. 893–901.
50. B. Pereda, Z. Aretxabaleta, and B. López: *J. Mater. Eng. Perform.*, 2015, vol. 24, pp. 1279–93.
51. C. Iparraguirre, A.I. Fernández, B. López, C. Scott, A. Rose, W. Kranendonk, B. Soenen, and G. Paul: *Mater. Sci. Forum*, 2005, vols. 500–501, pp. 677–84.
52. K.B. Kang, O. Kwon, W.B. Lee, and C.G. Park: *Scripta Mater.*, 1997, vol. 36, pp. 1303–08.